Predicted Influence of Organic Structure Directing Agents on Al Distributions in CHA Zeolites

Journal:	*Chemistry of Materials*
Manuscript ID	cm-2024-02463m.R2
Manuscript Type:	Article
Date Submitted by the Author:	n/a
Complete List of Authors:	Gao, Xuyao; University of Notre Dame, Chemical and Biomolecular Engineering Yeo, Steven; University of Notre Dame, Chemical and Biomolecular Engineering Gounder, Rajamani; Purdue University, Chemical Engineering Moini, Ahmad; BASF Environmental Catalyst and Metal Solutions Schneider, William; University of Notre Dame, Chemical and Biomolecular Engineering

Predicted Influence of Organic Structure Directing Agents on Al Distributions in CHA Zeolites

Xuyao Gao,[†] Steven Yeo,[†] Rajamani Gounder,[‡] Ahmad Moini,[¶] and William F. Schneider[*,†,§]

[†]*Department of Chemical and Biochemical Engineering, University of Notre Dame, Notre Dame, IN 46556, United States*

[‡]*Charles D. Davidson School of Chemical Engineering, Purdue University, West Lafayette, IN 47907, United States*

[¶]*BASF Environmental Catalyst and Metal Solutions, 25 Middlesex Essex Turnpike, Iselin, New Jersey 08830, United States*

[§]*Department of Chemistry and Biochemistry, University of Notre Dame, Notre Dame, IN 46556, United States*

E-mail: wschneider@nd.edu

Abstract

The distribution of Al on a zeolite framework can have a determining influence on chemical and catalytic properties. Those distributions are typically determined during synthesis as influenced by cationic organic structure directing agents (OSDAs). Here we use density functional theory (DFT) to compare the Al directing influence of N,N,N-trimethyl-1-adamantyl ammonium ($TMAda^+$), an OSDA commonly used to crystallize CHA zeolite, with four isomers that retain the adamantyl structure but relocate the

nitrogen center. Low energy configurations balance electrostatics-driven maximization of Al−Al and minimization of Al−N separations, the latter more important in OSDAs with more accessible charge centers. Statistical thermodynamics are used to predict thermal equilibrium Al distributions and corresponding Al pair features as a function of OSDA. All distributions differ from those predicted through naive application of Löwenstein's rule, disfavor the placement of two Al second-nearest-neighbor or within a single six-ring, and introduce different biases towards eight-membered rings and more remote Al. Results illustrate the potential to influence Al location through OSDA selection.

Introduction

Zeolites are a class of microporous crystalline materials composed of corner-sharing TO_4 (T = Si, Al) tetrahedra[1] that find wide use in catalysis, gas separations, and ion exchange.[2–4] More than 200 zeotypes are known,[5] and strategies to access a particular topology in the laboratory frequently rely on structure directing agents (SDAs)[6] which operate by templating the desired structure during crystallization.[7–10] The guest-host interaction energy between a target framework and a (typically) organic SDA (OSDA) can be used to rationalize observed crystallization patterns.[11] These computational methods have been used to extend the boundary of chemically synthesizable zeolites and to search for promising new OSDAs.[12–19]

The extent of incorporation and organization of heteroatoms provide additional control on zeolite properties. Aliovalent substitution of Si^{4+} by Al^{3+} ions introduces formal negative charges onto the zeolite framework (FW). Associated protons or extraframework, typically inorganic, cations can impart acidic or redox properties relevant to heterogeneous catalysis.[20] The proximity of these Al centers has been shown to have consequences for a range of physical and chemical properties of zeolites,[21,22] including for Brønsted-acid-catalyzed reactions[23] and the speciation and reactivity of charge-compensating cations.[24–29] These observations motivate efforts to control Al content and organization during synthesis.

In zeolites containing multiple symmetry-distinct tetrahedral (T-) sites, the choice of organic structure-directing agent (OSDA) can lead to the preferential occupation of specific T-sites with Al^{3+}, as observed through differential accessibility of probe molecules and various spectrocopies, in MTW,[30] MEI,[31] ISV,[32] FER,[33] IFR,[34] MSE,[35] and MFI.[36–39] In zeolites that present only a single symmetry-distinct T-site, the OSDA influence is manifested in the distribution and resultant proximity of Al^{3+}. Because of its practical catalytic relevance and high symmetry,[5] CHA zeolite is an ideal platform for observing these effects. CHA can be viewed as constructed from ABC stacking of double six-membered-ring (d6r) secondary building units (Figure 1(a)), creating cages connected by eight-membered-ring (8MR) windows. Experimental and computational evidence indicates that Co^{2+} titrations[40,41] and vibrational spectroscopy[23] are faithful reporters of six-membered-rings (6MR) containing two Al^{3+} centers. Such 6MR pair sites are absent in CHA crystallized with N,N,N-trimethyladamantan-1-aminium ($TMAda^+$; common name N,N,N-trimethyl-1-adamantyl ammonium) but present in CHA crystallization with N,N-dimethylcyclohexylammonium ($DMCHA^+$), albeit under different synthetic conditions.[42] Co-crystallization of CHA with $TMAda^+$ and Na^+[26,40,43,44] or Li^+[45] results in an enrichment in 6MR Al pairs, consistent with the computed tendency for Na^+ to site within the 6MR. Conversely, the K^+ co-crystallization is found to promote 8MR over 6MR Al pairs,[41] consistent with the preference for the larger K^+ cation to occupy these 8MR sites.

The energy of a framework of given Al content is observed to be both a function of Al arrangement and charge-compensating counterions. Early explorations of these ideas in ZSM-18[31] and ITQ-7,[32] based on density-functional-theory (DFT)-parameterized forcefields, found that charge compensation by protons or by charged OSDAs lead to different relative energies of Al arrangements. The Al−O−H vibrational spectra of zeolites crystallized with OSDAs and converted to the Brønsted form were more consistent with the Al arrangements expected based on the OSDA energies than the H^+-compensated energies, suggesting both the role of OSDA in guiding Al^{3+} siting and the persistence of that siting following OSDA

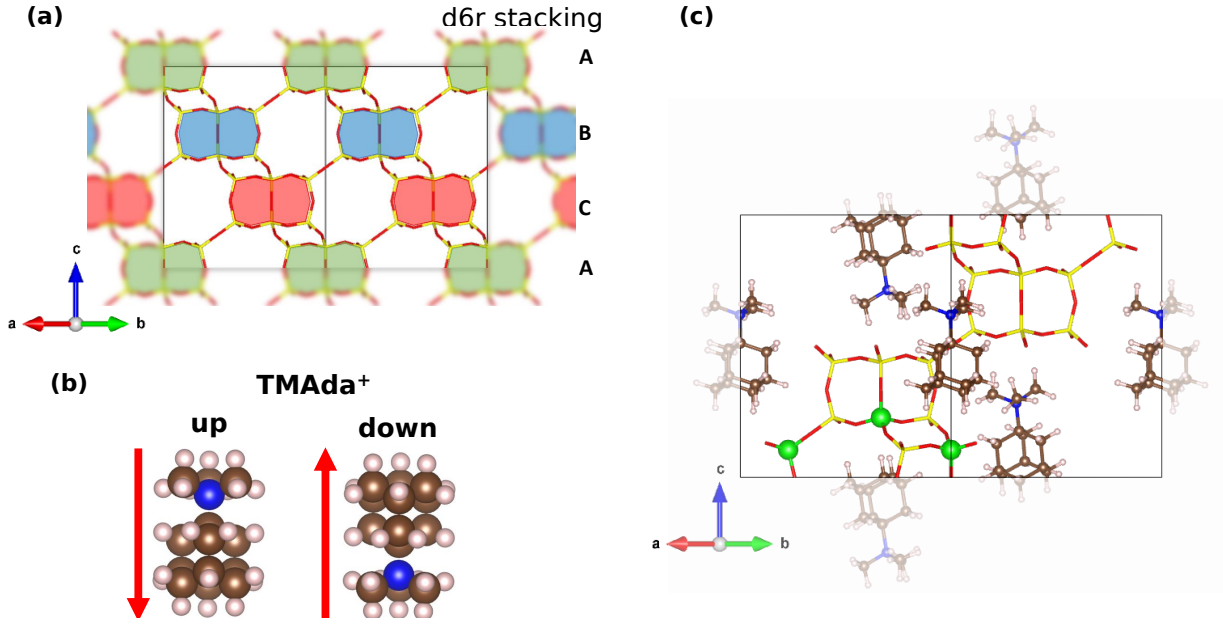

Figure 1: (a) Illustration of CHA stacked by 3 different layers of d6r building units, which are shaded in colors. (b) Possible up/down orientations of $TMAda^+$ when inside CHA cage. (c) Illustration of 36-T CHA with 3 Al substituted on the FW and 3 $TMAda^+$ are inserted in each of the 3 cages.

removal. DFT calculations similarly report that the CHA framework energy as a function of Al−Al separation is a strong function of the charge-compensating cations.[46,47] When charge compensated with protons, energies are minimized at first-nearest-neighbor (1NN, Al−O−Al) separation, demonstrating that Löwenstein's rule does not emerge from the energies of the protonated lattice. In a CHA cage occupied by $TMAda^+$, Al^{3+} has an energetic preference to site near the cationic tetramethylammonium end of the OSDA, consistent with an electrostatic influence on Al^{3+} distribution.[48] The configurational energy reported by DFT[44] or a DFT-trained classical forcefield[49] on CHA frameworks filled with one $TMAda^+$ per cage indicate that Al configurations that place two Al within the same 6MR are energetically unfavorable, consistent with experimental observations that these features are rare on CHA zeolite prepared with $TMAda^+$ as the sole SDA. A negative correlation between the reciprocal Al−N distance and configurational energy is consistent again with a significant if not dominant role of electrostatics in guiding Al^{3+} distributions, an effect that appears

to be screened but not altered with the consideration of the potential screening influence of water.[48] The energy of first-nearest-neighbor Al−O−Al linkages increases significantly when charge compensated by $TMAda^+$, in both models with and without explicit water,[50] providing a rationale for the experimentally observed Löwenstein's's rule.[51] These results suggest the potential to influence Al^{3+} siting by altering the charge distribution on OSDAs. Recent calculations show that the low-energy location of a single, isolated Al^{3+} within a large *cha* supercell can be altered by adjusting the location of the nitrogen charge center on a co-occluded $TMAda^+$ mimic.[52]

Here we extend these ideas by exploring the influence on global Al^{3+} distributions of a family of $TMAda^+$ mimics modified to relocate or further expose the charge center. We use DFT to compute the energies of the full set of symmetry-distinct Al configurations possible within a three cage CHA unit cell at Si/Al = 11 across $TMAda^+$ and four mimics. We find that the energy distributions and even the absolute OSDA exchange energies are a strong function of OSDA. Further, by fingerprinting configurations according to Al pair types and averaging over configurations likely accessible at synthetic conditions, we find that all OSDAs, including $TMAda^+$ itself, bias against second-nearest-neighbor Al pairs, thus against all 4MR pairs, against all 6MR pairs, and bias for or against 8MR pairs and isolate Al (those not sharing a common ring with another Al^{3+}) to varying extents. These differences can be traced to the accessibility of OSDA charge centers to framework T-sites as well as the preference for Al^{3+} to maximize separation. They more than counterbalance the driving force for Al^{3+} to aggregate in the proton-compensated form.[46,47] Results illustrate the potential to bias Al distributions and thus chemical properties through OSDA charge modifications.

Methods

Density functional theory (DFT) calculations were performed on a 36 T-site CHA hexagonal unit cell using the Vienna Ab initio Simulation Package (VASP),[53] version 5.4.1. Lattice constants were obtained from the Database of Zeolite Structures (IZA).[5] Core–valence interactions were treated using the projector augmented wave (PAW) methods,[54] exchange and correlation treated within the Perdew–Burke–Ernzerhof (PBE) generalized gradient approximation (GGA),[55] and the DFT model augmented with the D3 method to describe van der Waals interactions.[56] Plane waves were included to a 400 eV cutoff and the first Brillouin zone sampled at the Γ point. Self-consistent field (SCF) electronic energies and forces were converging to 1×10^{-5} eV and 0.01 eV/Å, respectively. The zeolite framework was held rigid and OSDA relaxed in all simulations[44,49]). The electrostatic potentials of free OSDAs were computed with with B3LYP functional and 3-21+G basis set in Gaussian.[57]

Symmetry-distinct Al configurations were constructed using the SOD (Site-Occupation Disorder).[58] Avogadro,[59] the Atomic Simulation Environment,[60] and the Zeolite Simulation Environment[61,62] were used to construct OSDAs and generate initial structures of the Al-substituted, OSDA-occluded CHA.

Results and Discussions

Figure 2 illustrates the 2D and 3D structure of $TMAda^+$ and the four variants probed here. $TMAda^+$ is constructed of adamantyl and trimethylammonium groups. To generate structurally similar OSDAs with altered charge distributions, we moved the cationic N center to each of the three symmetry-distinct carbon centers of the adamantyl group, creating the quarternary amine 1-(tert-butyl)-1-azaadamantan-1-ium (m1), tertiary 3-(tert-butyl)-1-azaadamantan-1-ium (m3), and secondary 5-(tert-butyl)-2-azaadamantan-2-ium (m2). A fourth variant, N,N-dimethyladamantan-1-aminium (m4), was created by replacing a trimethylammonium methyl with a hydrogen. Figure 2 reports computed electrostatic potentials of

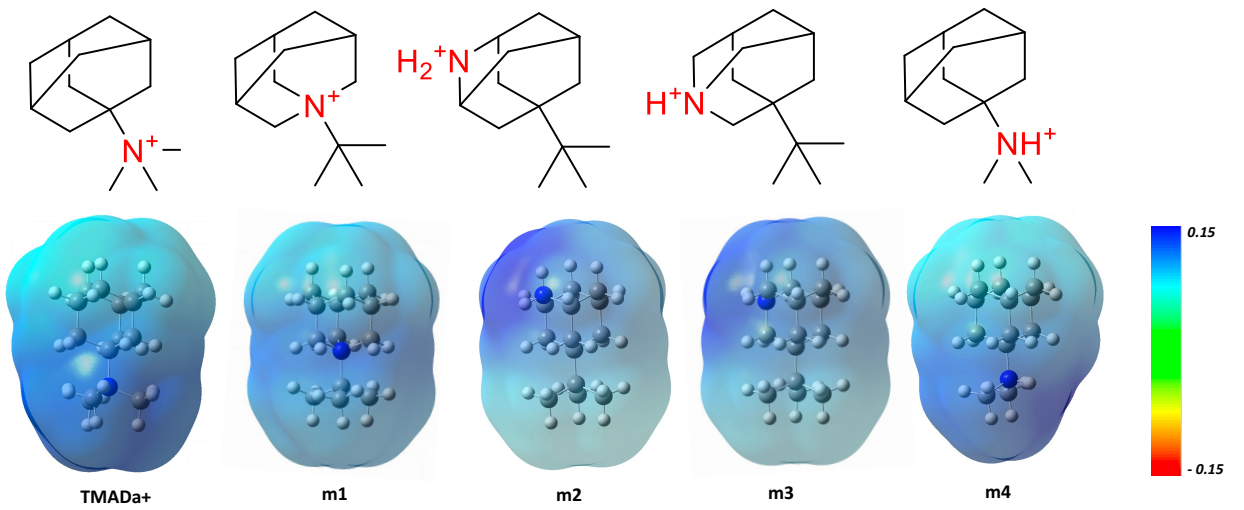

Figure 2: (top) 2D representations of TMAda$^+$ and four structural modifications. (bottom) DFT-optimized structures overlayed with molecular electrostatic potential color-mapped onto electron density surface (isovalue = 0.00004). Electrostatic potential scale in au at right; positive regions are attractive to a negative test charge.

the free OSDAs, showing that both the location and intensity of the positive potential region (that is expected to be attractive to an anionic framework) vary substantially with ammonium location. While rare, non-quaternary ammoniums are not unprecedented as OSDAs,[33] although other considerations, including solubility and hydrothermal stability, are also relevant to the practical utility of an OSDA. These particular choices are motivated by the desire to mimic to the maximum extent possible the precise fit within the CHA cage that restrict TMAda$^+$ itself to only two possible orientations within a CHA cage[19](Figure 1(b)), as well as imposing a systematic variation in charge location.

We consider a 36 T-site CHA hexagonal unit cell (Figure 1(c)) which, when decorated with three Al^{3+}, has an effective Si/Al ratio of 11, or on average one Al^{3+} per d6r. Eleven is the lowest achievable Si/Al ratio assuming every cage is filled with a monocationic OSDA, charge balance is perfect, and no other anionic centers are present. As every T site is shared by three cages, every cage in this model "sees" three Al. We identified 139 symmetry-distinct configurations of three Al locations on the framework,[58] excluding configurations that violate Löwenstein's rule, thus ensuring no Al pairs are first nearest neighbors. We fill the three

CHA cages with three of the same OSDA molecules from Figure 2. Assuming that each OSDA is constrained to one of two distinct orientations ("up" and "down") leads to $2^3 = 8$ possible OSDA orderings and a total of $8 \cdot 139 = 1112$ total Al/OSDA configurations per OSDA type.

Extensive calculations on a charge-neutral analog of $TMAda^+$ in a fully siliceous CHA show that the OSDA has a strong preference to align its principal axis along the *c* axis of CHA with the central atom of the trimethyl group ± 1.7 Å from the center of the CHA cage.[19] We initialized all the OSDAs here using this same orientation, and find that all OSDAs fit within the *cha* cage in only two orientations. Further, in previous work,[49] we compared the energy predictions of models in which the zeolite framework was held rigid or relaxed. While energy differences are compressed in the latter case, general energy orderings are unchanged. More importantly, the rigid model is successful in recovering experimental Al distribution observations for CHA synthesized with $TMAda^+$ alone[49] and with Na^+.[44]

While $TMAda^+$ and m1 have a three-fold axis of symmetry, m2, m3, and m4 do not. To test the sensitivity of configurational energies to rotation about the principal axis, we selected six m3 configurations from the 1112 and computed energies as a function of the rotation angle. Each OSDA in a specific Al configuration and OSDA ordering has the potential to rotate 360° around its long axis (Figure 3(a,b)). The rotation space was divided into eight distinct self-rotation angles, in 45° intervals. Consequently, there are a total of 8^3 possible combinations of the 3 OSDA systems with varying OSDA self-rotation angles, each resulting in a different average Al−N distance. From these combinations, 12 representative configurations were selected, covering the majority of average Al−N distances in the system. Figure 3(c) reports the energies of six distinct Al/m3 OSDA configurations, each at twelve different values of rotational angles, against average reciprocal Al−N distance. Offsets between datasets reflect the different intrinsic energies of particular Al^{3+}/OSDA configurations, and the variation within a dataset indicates the magnitude of the internal rotation influence. Energies are minimized at rotational angles that maximize the reciprocal Al−N distance, and we use this

observation to initialize all the lower-symmetry configurations.

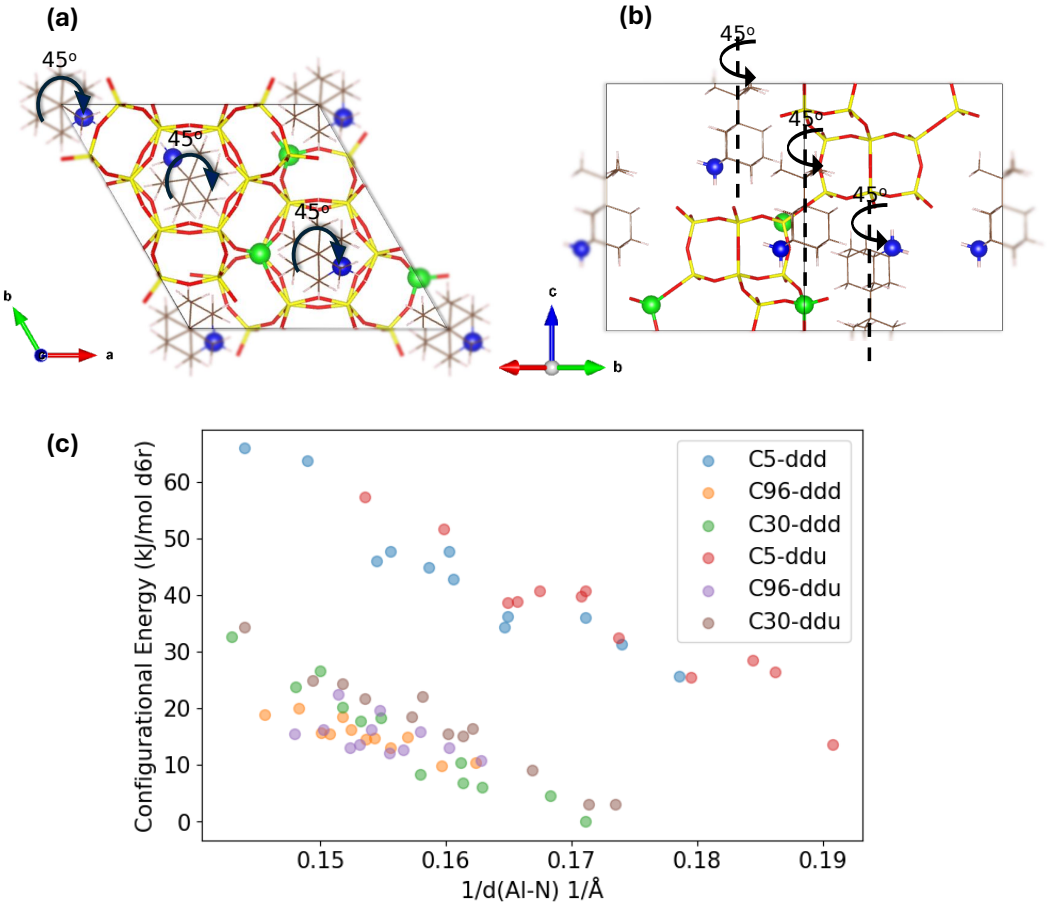

Figure 3: (a) Top and (b) side view of m3 OSDA and rotational degrees of freedom within the CHA cage. (c) Configurational energy vs average reciprocal Al−N distance of six unique Al configurations and OSDA orderings at twelve different rotations. Legend reports OSDA ordering and Al configuration ID in the Zenodo data repository.

We relaxed all structures; the final configurations and their energies are provided in a Zenodo data repository.[63] For analysis purposes, we set the energy of the lowest-energy 3Al/TMAda$^+$ configuration to zero and report a histogram of all TMAda$^+$ energies in the first column of Figure 4, binned by 2 kJ mol$^{-1}_{\text{d6r}}$. The lowest energy configuration is identical to that identified previously with classical models.[49] TMAda$^+$ energies span approximately 70 kJ mol$^{-1}_{\text{d6r}}$, 10 kJ mol$^{-1}_{\text{d6r}}$ greater than those classical results.[49] Most configurations lie between 10 kJ mol$^{-1}_{\text{d6r}}$ to 30 kJ mol$^{-1}_{\text{d6r}}$ above the minimum energy configuration.

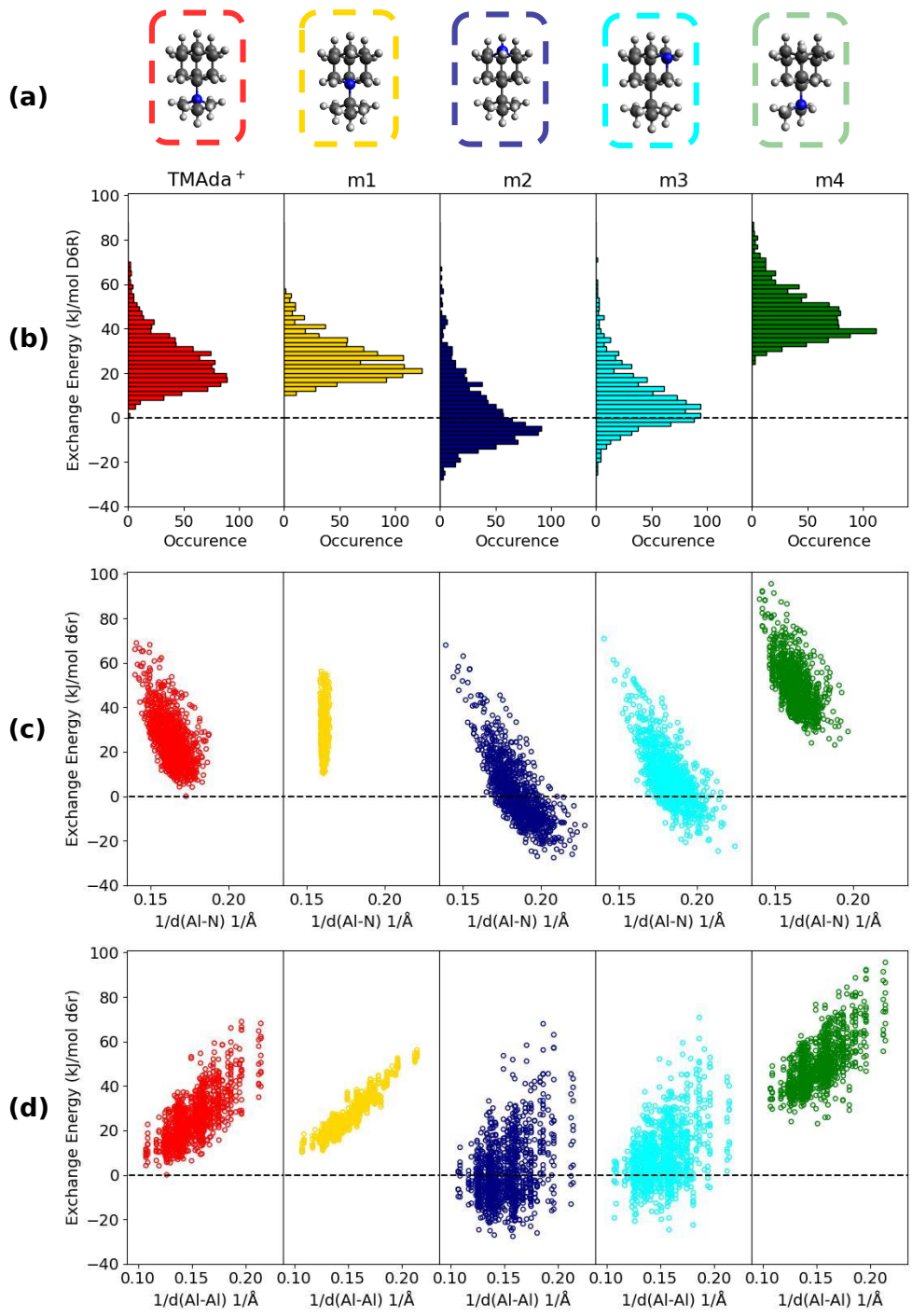

Figure 4: (a) Illustrations of $TMAda^+$ and four modifications. Histograms of (b) OSDA exchange energies referenced to lowest-energy $TMAda^+$ configuration, (c) OSDA exchange energies against mean reciprocal Al−Al distance, and (d) OSDA exchange energies against mean reciprocal Al−N distance. Red, yellow ,dark blue, cyan and green represent $TMAda^+$, m1, m2, m3 and m4.

To compare across OSDAs, we define an exchange reaction and corresponding OSDA exchange energy $\Delta E_{\mathrm{ex}}^{i,j}$ for a given OSDA TMAda-mi^+ and Al/OSDA configuration j according to:

$$\mathrm{CHA/3\,TMAda^+ + 3\,TMAda\text{-}m}i^+ \longrightarrow \mathrm{CHA/3\,TMAda\text{-}m}i^+ + \mathrm{3\,TMAda^+} \quad (1)$$

$$\Delta E_{\mathrm{ex}}^{i,j} = (E^{i,j} - E_{\mathrm{min}}^{\mathrm{CHA/TMAda+}})/3 - (E^{\mathrm{TMAda\text{-}m}i+} - E^{\mathrm{TMAda+}}) \quad (2)$$

where $E^{i,j}$ is the total DFT energy of the specific Al distribution and OSDA ordering, $E_{\mathrm{min}}^{\mathrm{CHA/TMAda+}}$ is the DFT energy of the lowest-energy 3Al/TMAda$^+$ configuration, $E^{\mathrm{TMAda+}}$ and $E^{\mathrm{CHA/TMAda\text{-}m}i+}$ are the total energies of isolated TMAda$^+$ and TMAda-mi^+ computed in an empty 36-T CHA unit cell with a charge-compensating background charge, and the factor of 1/3 provides a normalization to d6r. OSDA exchange energy histograms are reported in Figure 4(b), binned by $2\,\mathrm{kJ\,mol_{d6r}^{-1}}$.

Two trends are immediately evident. First, in all cases OSDA exchange energies are sensitive both to Al configuration and OSDA orientation. Thus, different Al distributions minimize energy for each of the OSDAs. Further, the widths of the energy distributions vary considerably, likely reflecting differences in access of the OSDA charge centers to framework Al. Second, the energy distributions are shifted relatively to one another by upwards of $40\,\mathrm{kJ\,mol_{d6r}^{-1}}$. The m1 distribution is narrower and begins $10\,\mathrm{kJ\,mol_{d6r}^{-1}}$ above that of TMAda$^+$, while m2 and m3 distributions are wider and begin nearly $-20\,\mathrm{kJ\,mol_{d6r}^{-1}}$ below TMAda$^+$. The m4 distribution is comparable to but shifted $20\,\mathrm{kJ\,mol_{d6r}^{-1}}$ upward from TMAda$^+$.

The guest-host interaction energies (GHIE) between charge-neutral OSDA surrogates—constructed by replacing nitrogen centers with carbon—and a completely siliceous framework are commonly used to report on the structure-directing capacity of an OSDA.[11–13,19,34,64] By construction, the uncharged GHIEs of TMAda$^+$, m1, m2, and m3 with CHA are identical. Thus, the shifts in the computed OSDA exchange energy histograms between these four reflect differential structure directing capacity associated with differences in location

of nitrogen centers. To explore these differences, we plot in Figure 4(c) and (d) the OSDA exchange energy against the mean reciprocal Al−N and Al−Al distances, averaged over the three closest respective contacts. OSDA exchange energies of OSDA m1, which from Figure 2 has the least accessible charge center, correlate strongly with Al−Al separations, while Al−N separation is invariant across all structures. In contrast, the OSDA exchange energies of $TMAda^+$ and its modifications m2 and m3, which expose the OSDA charge center at different locations, correlates most strongly with the reciprocal Al−N separations. The large shift downward in OSDA exchange energy of the latter two relative to $TMAda^+$ is correlated with the closer approach of OSDA nitrogen charge centers to framework Al, and the greater dispersion in OSDA exchange energies is associated with a larger overall range in Al−N separations. That energies correlate with reciprocal distances suggests a largely electrostatic origin to the differences. Consistent with this observation, the dispersion contribution to the PBE+D3 energy is constant across configurations. The results reflect the dominant contribution of electrostatics to overall OSDA-framework interaction energies.

In contrast to the other mimics, OSDA m4 differs from $TMAda^+$ by one ammonium methyl group and thus has a different uncharged GHIE. We compute the GHIE of uncharged m4 with CHA to be $18\,\mathrm{kJ\,mol}_{\mathrm{d6r}}^{-1}$ less negative than that of $TMAda^+$ and the other three mimics, consistent with the offset shown in Figure 4. Further, both the reciprocal Al−Al and Al−N correlations of m4 and $TMAda^+$ are similar. Thus, uncharged GHIE appear to be the largest discriminator between $TMAda^+$ and m4. The set of $TMAda^+$ and its four structure modifications thus nicely span a range of behaviors influencing the absolute value and dispersion of OSDA-framework interaction energies.

To further surface the various contributions to the DFT-computed OSDA exchange energies, we computed the energy of the Si/Al 11 CHA framework with various Al distributions j compensated by a uniform background charge $E^{\mathrm{bg},j}$. Structures and their corresponding $E^{\mathrm{bg},j}$ are available in a Zenodo data repository.[63] As shown in Figure 5(a), $E^{\mathrm{bg},j}$ spans $50\,\mathrm{kJ\,mol}_{\mathrm{d6r}}^{-1}$ and is strongly correlated with the mean reciprocal Al−Al distance, reflecting an intrinsic

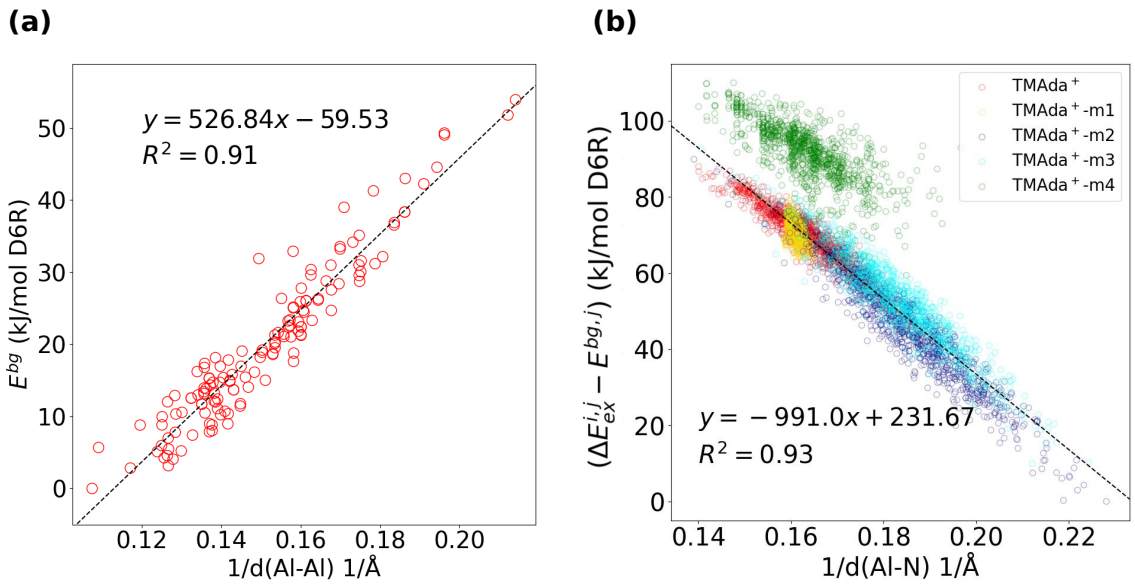

Figure 5: (a) Uncompensated FW energies E^{bg} vs mean reciprocal Al−Al distance. (b) $\Delta E_{\mathrm{ex}}^{i,j} - E^{bg}$ vs mean reciprocal Al−N distance. In both cases, lowest energy configurations are shifted to zero. Black dashed line is best fit to non-TMAda$^+$-m4 energies.

electrostatic driving force for unscreened anionic Al centers to be remote from one another. Figure 5(b) reports the OSDA exchange energies minus the underlying Al−Al repulsion, $(\Delta E_{\mathrm{ex}}^{i,j} - E^{\mathrm{bg},j})$ vs mean reciprocal Al−N distance. Overall energies span 110 kJ mol$_{\mathrm{d6r}}^{-1}$, cluster into groups for each OSDA, and are strongly anti-correlated with mean reciprocal Al−N distance. OSDA m4 is further offset by about 18 kJ mol$_{\mathrm{d6r}}^{-1}$ from TMAda$^+$, m1, m2, and m3, consistent with the differences in uncharged GHIE. Figure 5 thus shows that framework electrostatics, neutral guest-host interaction energies, and specific charge-charge interactions between OSDA and framework all contribute to the DFT OSDA exchange energies.

To relate these energy histograms to underlying Al configurations, we fingerprinted each Al configuration by the Al pair features shown in Figure 6, chosen because these features are most relevant to ion exchange and catalytic function.[26,40,43] Seventeen unique Al−Al separations are possible on the rigid CHA framework within 8.1 Å, and those 17 map onto the nine pair types shown in Figure 6, including eight involving a single ring and one type that spans two different rings, which we label 3NNXR (third-nearest-neighbor cross-ring);

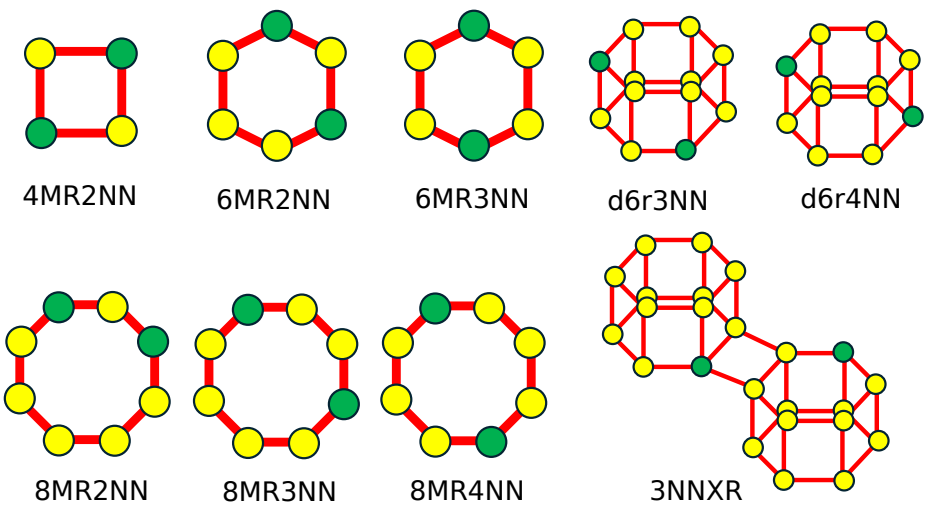

Figure 6: Al pair features used to characterize Al distributions. Yellow and green circles represent Si and Al atoms, respectively, and red lines represent bridging oxygen. Each feature is named by their ring strucutres (aMR: a membered-ring where a = 4, 6, 8, XR: cross ring, d6r: double six ring) and Al proximity (bNN: bth nearest-neighbor where b = 2, 3 or 4)

pairs at distances greater than 8.1 Å are assigned as remote. We identified the three unique pairs in each 36 T-site CHA unit cell using the minimum image convention and assigned each of the three to one of these categories.

To illustrate the potential influence of OSDA on observable Al features, we assume that OSDA up/down ordering is random (Figure 1 (b)), hypothesized to be representative of synthetic conditions, and compute the algebraic average energies across OSDA ordering for each unique Al configuration. Figure 7 reports the pair fingerprints of the ten lowest- and ten highest-energy configurations for $TMAda^+$. Columns indicate symmetry-distinct pair features and are arranged from shortest (second-nearest-neighbor in a four-membered ring, or 4MR2NN) to longest (fourth-nearest-neighbor in an eight-membered ring, or 8MR4NN) pair feature, including three symmetry-distinct features that span two different rings (3NNXR). Numbers indicate the frequency of appearance of that feature in that configuration. A value greater than one indicates multiple occurances of the same feature, not necessarily in the same ring. As example, the bottom row in Figure 7 corresponds to a configuration in which

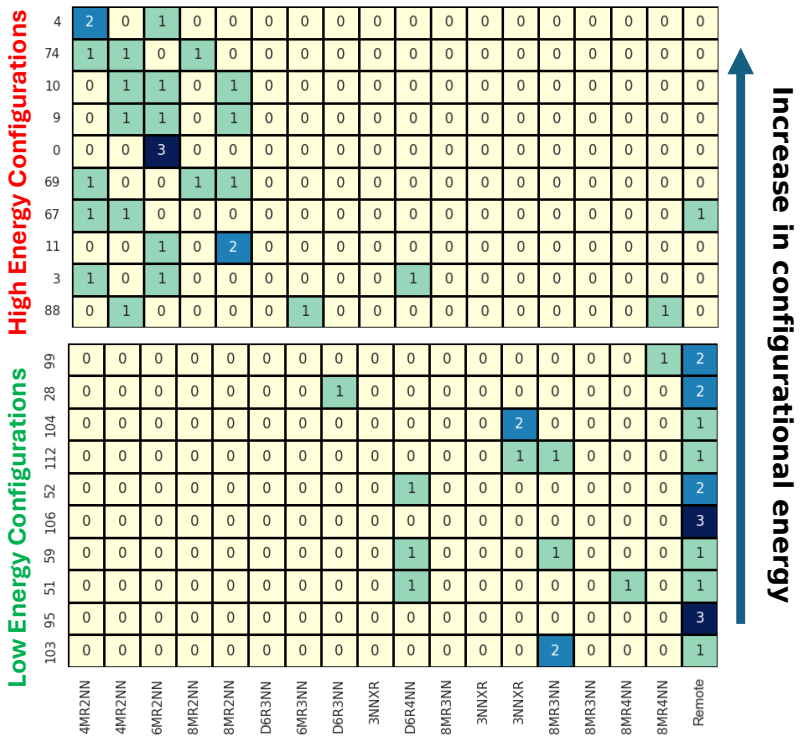

Figure 7: Al pair fingerprints of the ten lowest and ten highest average energy Al configurations in the field of randomly oriented $TMAda^+$. Numbers in each row indicate the occurrence of each distinct Al pair fingerprint. Configuration numbers refer to entries in the Zenodo data repository.

the three Al form two distinct 8MR3NN pairs in different 8-rings and a third pair of remote Al. As is evident from Figure 7, the low energy configurations are dominated by those that present the most remote, non-ring-sharing Al. Second-nearest-neighbor (2NN) of all types as well as 6MR pairs are absent within the low energy manifold, and d6r and 8MR pairs make only scattered appearance. In contrast, the high energy manifold is dominated by 2NN pairs; at least two such pairs are present in all of the top ten energy configurations.

The absence of 6MR Al pairs from the low-energy manifold in Figure 7 is consistent with the experimental observation, based on Co^{2+} titrations, that CHA crystallized with $TMAda^+$ contains no such pairs.[44] The absence of 2NN Al pairs is similarly consistent with the low intensity of the Q4(2Al) peak in ^{29}Si nuclear magnetic resonance spectra.[40,44] To relate calculations to the driving force for a particular ordering at finite temperature

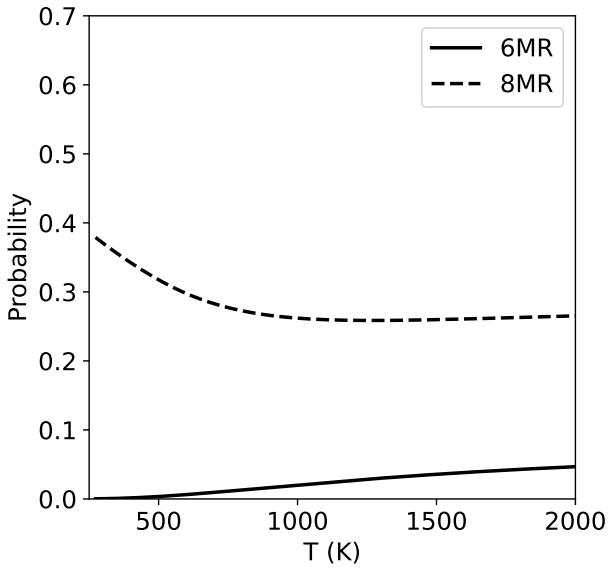

Figure 8: Boltzmann-weighted probability of occurrence of 8MR or 6MR Al pairs as a function of temperature in field of $TMAda^+$.

synthetic conditions, we plot in Figure 8 the Boltzmann-weighted probabilities of 6MR and 8MR Al pairs based on the configurational energies of Figure 7 and giving 1/3 weight to each pair type in a given configuration.[49] The probability of 6MR Al pairs remains essentially zero up to common synthetic temperatures of 443 K; only at temperatures above 500 K do 6MR pair probabilities begin to rise. 8MR pairs exhibit the opposite dependence, declining in probability with increasing temperature up to very high temperature.

Figure 9(a) reports the distribution of feature types assuming that all configurations are equally probable, thus consistent with Löwenstein's rule[51] forbidding 1NN pairs. As noted previously,[41] Löwenstein's rule predicts non-zero populations of 2NN pairs as well as significant fractions of 6MR pairs, as well as d6r and cross-ring (XR) pairs. For comparison, we computed the energies of all unique three Al arrangements in the 36 T-site unit cell, replacing OSDAs with a charge-compensating background charge. Figure 9(b) reports the distribution of feature types based on a 443 K Boltzmann weighting of these OSDA-free framework configurations. Under this OSDA-free bias, Al seek to be remote from one another, 2NN pairs have vanishing and 3NN pairs small probabilities, and the remote feature dominates

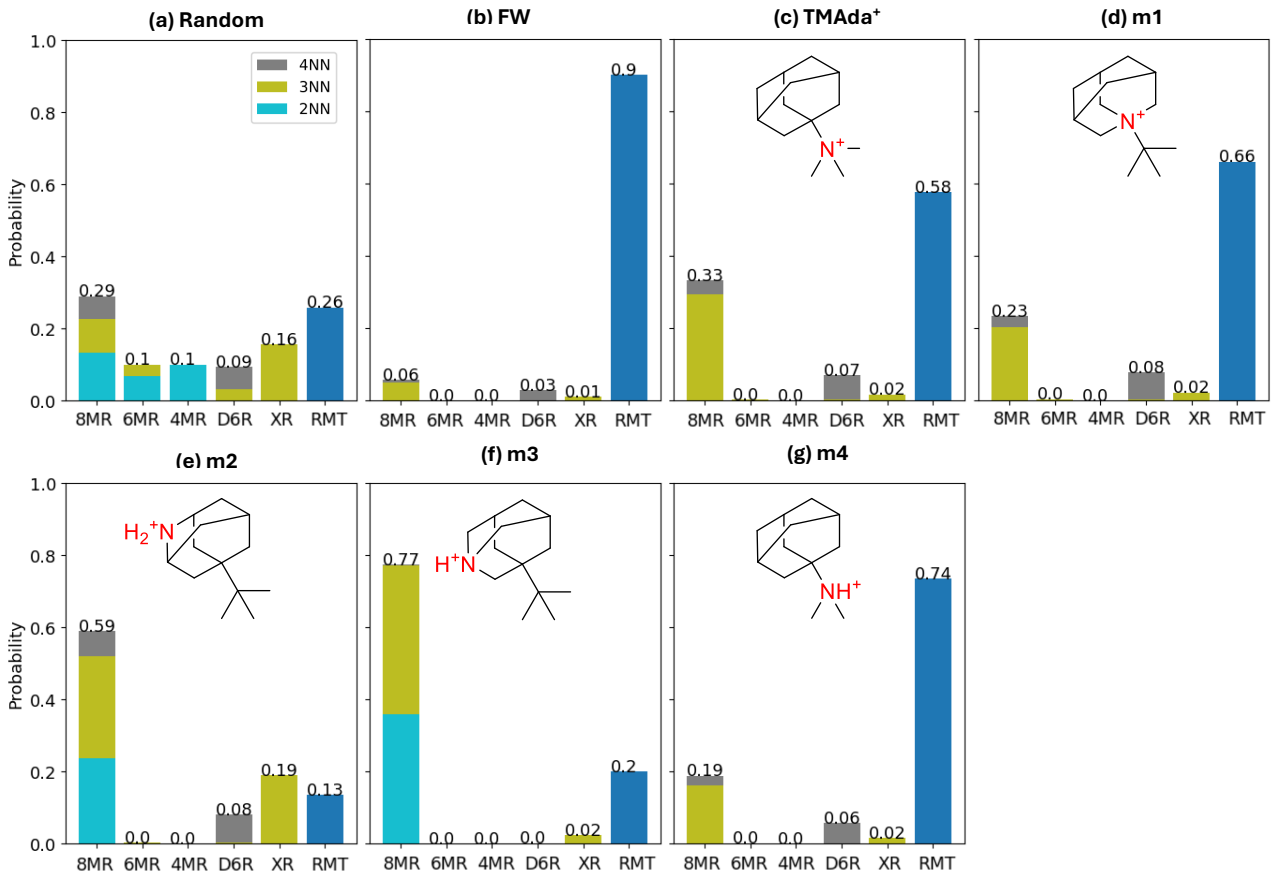

Figure 9: Al pairing feature distributions based on (a) random distribution excluding 1NN Al pairs; (b) OSDA-free framework energy; (c) CHA-TMAda$^+$ energy; (d) CHA-m1 energy; (e) CHA-m2 energy; (f) CHA-m3 energy; and (g) CHA-m4 energy. Probabilities based on 443 K Boltzmann weightings. XR and RMT refer to cross-ring and remote pairs.

the distribution, consistent with previous prediction.[41] Figure 9(c) reports predictions based on the TMAda$^+$ energies of Figure 4, again Boltzmann weighted at 443 K. Consistent with Figure 7 and with previous reports,[44,49] TMAda$^+$ is predicted to bias against all 2NN[40,44] and 6MR pairs, with a mix of 8MR and remote pairs consistent with Figure 8.

Figure 10 reports the fingerprints of the ten lowest- and ten highest-energy Al configurations in the fields of the four modifications on TMAda$^+$ (averaged over OSDA orientations). It is evident that OSDA modification does have a significant impact not only on absolute energies (Figure 4(b)) but also on the relative energies of Al arrangements. There are some similarities, however: 4MR and 6MR pairs are absent in the low-energy manifold of all five OSDAs, while the high energy manifold has a large occurrence of 4MR 2NN features.

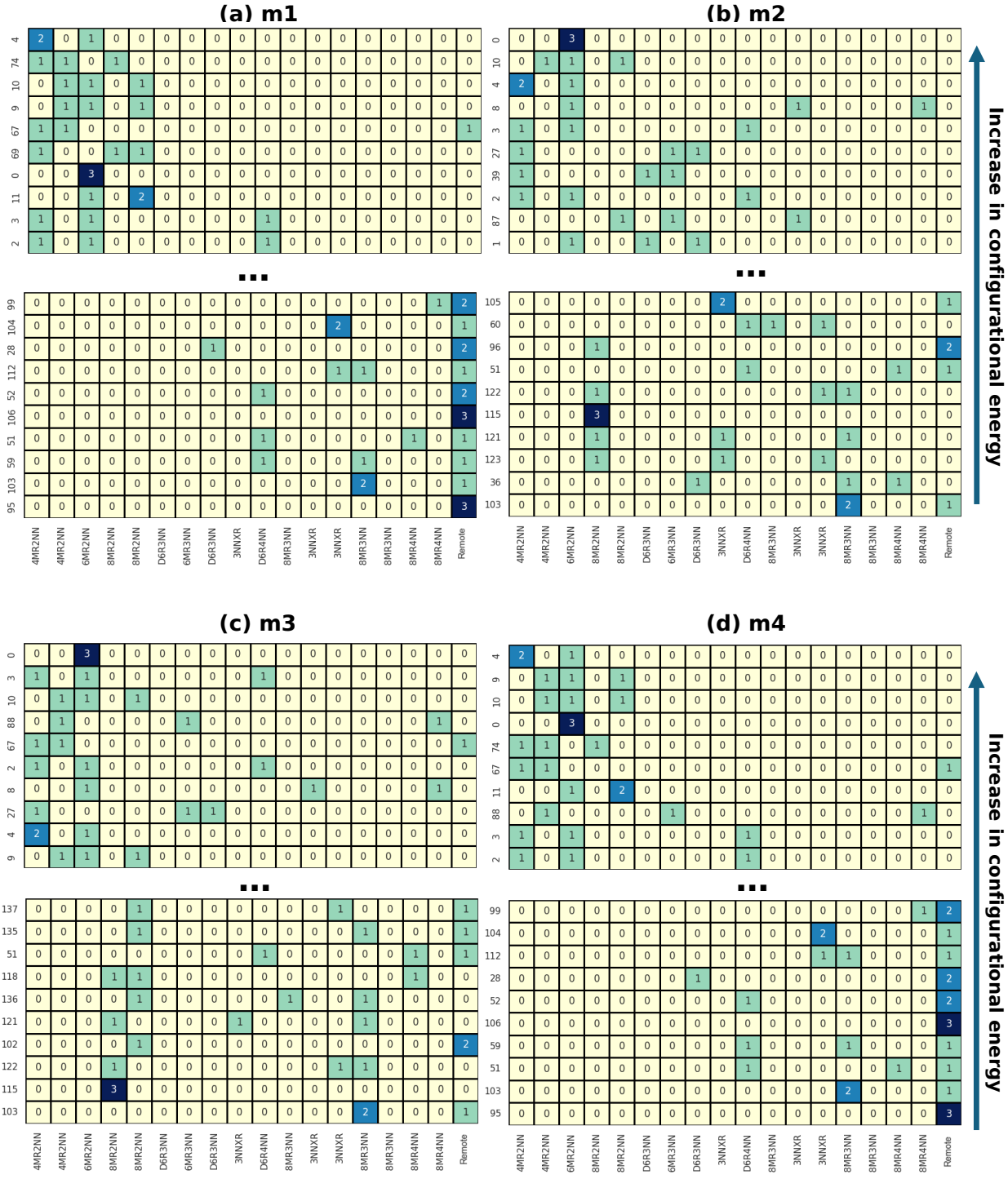

Figure 10: Al pair fingerprints of the ten lowest and ten highest average energy Al configurations in the field of randomly oriented (a) m1, (b) m2, (c) m3 and (d) m4. Numbers in each row indicate the occurrence of each distinct Al pair fingerprint. Configuration numbers refer to entries in the Zenodo data repository.

3NNXR features are rare in the low and high energy manifolds, evidently more common at intermediate energies.

In the field of the quaternary amine 1-(tert-butyl)-1-azaadamantan-1-ium (m1), low energy configurations share features with $TMAda^+$ itself: the two lowest energy configurations are identical, remote features are strongly favored, and 2NN features are absent (Figure 10). Similar to $TMAda^+$ within the high-energy configurations, 2NN features are common. The primary difference between $TMAda^+$ and m1, then, is the width of the energy distribution, shown in Figure 4(b). As a result, and as shown in Figure 9(d), the Boltzmann-weighted feature distribution in the presence of m1 is similar to $TMAda^+$, the only difference being a small shift in bias from 8MR towards remote Al pairs. OSDA m1 would be expected to produce CHA with an Al distribution essentially indistinguishable from $TMAda^+$, and based on the energy offset in Figure 4(b), to be a somewhat less effective structure directing agent.

More substantial differences are evident for the secondary amine 5-(tert-butyl)-2-azaadamantan-2-ium (m2) OSDA (Figure 10). 2NN fingerprints begin to appear in the low energy window, at the expense of long-range Al pairs. Similarly, the high energy window contains more configurations with Al pairs at greater distances than 2NN. The aggregate effect is most clearly seen in Figure 9(e): in the presence of m2, CHA is expected to be enriched in 3NN8MR and even 2NN8MR pairs relative to $TMAda^+$ or even the Löwenstein's rule distribution, while 6MR pairs are expected to be uncommon. Further, the energy offset in Figure 4(b) suggests that m2, at least if present in the protonated form, would be a strong director towards CHA with this distribution.

The configurational biases introduced by tertiary amine 3-(tert-butyl)-1-azaadamantan-1-ium (m3) OSDA are similar to those introduced by OSDA m2, but with an even greater appearance of 8MR pairs at the expense of the minority d6r and XR pairs (Figure 10(c)). These differences are reflected in Figure 9(e), where 2NN and 3NN8MR pairs are highly enriched at the expense of d6r, XR pairs, and 4NN8MR pairs, all of which are nearly absent.

The tertiary amine N,N-dimethyladamantan-1-aminium (m4), created by removing a

methyl group from $TMAda^+$, might be expected to differ most dramatically in Al directing tendencies from the other four OSDAs. Rather, its low and high energy configuration manifolds (Figure 10) are similar to m1 and even $TMAda^+$ itself. 2NN pairs are again absent among low energy configurations and prominent among high energy ones. Its feature distribution (Figure 9) reflects these similarities, with 8MR pairs and remote Al being the only features of significant population, and the remote Al being most pronounced. Thus, OSDA m4 is expected to crystallize CHA with an Al distribution similar to $TMAda^+$ but, given its poorer neutral guest-host interactions, to be less effective in promoting the CHA structure overall.

Conclusions

In this work, we explore the consequences of explicit inclusion of cationic OSDAs and anionic framework Al centers in the guest-host interaction evaluation. Starting from the CHA-$TMAda^+$ system, we consider $TMAda^+$ and OSDA mimics constructed to have charge-neutral interaction energies identical to $TMAda^+$ itself but to present different charge distributions. We evaluate energies within this space using first principles calculations. Predicted relationships between Al configuration and $TMAda^+$-compensated energy are consistent with classical results.[49] We find that not only do relative Al configurational energies respond to modifications of the OSDA, but absolute interaction energies themselves shift substantially, suggesting that charge-neutral surrogates may miss an important contribution to the templating ability of an OSDA.

To characterize the influence of charge distribution on Al siting, we fingerprint Al configurations by Al−Al pair types. Certain features, such as the tendency to disfavor 4MR and 6MR Al pairs, while other features, especially the populations of 8MR Al pairs, are highly responsive to OSDA charge distribution. OSDAs with less accessible OSDA charge centers, thus exhibiting larger mean Al−N separations, tend to favor configurations that maximally

separate Al. In contrast, OSDAs with more accessible charge centers promote a closer Al approach, including even 2NN Al pairs in 8MRs. Such changes in distribution could manifest, for instance, in differing abilities to host Cu dimers relevant to partial methane oxidation[65] or in the pairability of solvated Cu ions relevant to NO_x selective catalytic reduction.[66]

The non-quaternary $TMAda^+$ mimics studied here are likely incompatible with zeolite synthesis in basic media. They may be more compatible with (and have strong structure directing properties at) the lower pH typical of synthesis in fluoride media or from solid silica at near neutral pH.[67] Evidence suggests that non-quaternary ammoniums may also be useful as secondary OSDA partners to a primary OSDA,[33] and such a strategy may be a viable approach to realizing some of the differential directing ability of the $TMAda^+$ mimics. The discovery of OSDAs that offer Al siting control and are compatible with basic synthesis conditions remains an opportunity. Extensions of these ideas to lower symmetry zeolite frameworks and less orientationally constrained OSDAs present practical but not conceptual computational challenges. The work here highlights the potential opportunities to realize strategies to control both zeotype and Al distribution through OSDA selection.

Data Availability

The data that support the findings of this study including sample VASP input files for energy evaluations, all final optimized structures and their corresponding potential energies for CHA-OSDA pairs, the charged CHA frameworks, and charged isolated OSDAs, all shared in the Zenodo data repository available at `https://doi.org/10.5281/zenodo.13236662`.

Acknowledgements

The authors gratefully acknowledge financial support from the CBET-DMREF program under award number 1922154. They further thank Drs. Subramanian Prasad, Vivek Vattipalli, and Anthony Debellis, BASF, and Drs. Edward Maginn and Craig Waitt, University of

Notre Dame, for helpful discussions and input. The computing resources for this work were provided by the Notre Dame Center for Research Computing.

References

(1) Corma, A. State of the art and future challenges of zeolites as catalysts. *J. Catal.* **2003**, *216*, 298–312.

(2) Breck, D. W. *Zeolite molecular sieves: structure, chemistry, and use*; John Wiley & Sons, 1973.

(3) Flanigen, E.; Jansen, J.; van Bekkum, H. *Introduction to Zeolite Science and Practice*; Elsevier Science, 1991.

(4) Speybroeck, V. V.; Hemelsoet, K.; Joos, L.; Waroquier, M.; Bell, R. G.; Catlow, C. R. A. Advances in theory and their application within the field of zeolite chemistry. *Chem. Soc. Rev.* **2015**, *44*, 7044–7111.

(5) Baerlocher, C.; McCusker, L. Database of Zeolite Structures. `http://www.iza-structure.org/databases/`, 2008; Accessed: 2024-10-01.

(6) Moliner, M.; Rey, F.; Corma, A. Towards the rational design of efficient organic structure-directing agents for zeolite synthesis. *Angew. Chem., Int. Ed.* **2013**, *52*, 13880–13889.

(7) Gies, H.; Marker, B. The structure-controlling role of organic templates for the synthesis of porosils in the systems SiO2/template/H2O. *Zeolites* **1992**, *12*, 42–49.

(8) Gies, H. In *Advanced Zeolite Science and Applications*; Jansen, J., Stöcker, M., Karge, H., Weitkamp, J., Eds.; Studies in Surface Science and Catalysis; Elsevier, 1994; Vol. 85; pp 295–327.

(9) Kubota, Y.; Helmkamp, M. M.; Zones, S. I.; Davis, M. E. Properties of organic cations that lead to the structure-direction of high-silica molecular sieves. *Microporous Mater.* **1996**, *6*, 213–229.

(10) Wagner, P.; Nakagawa, Y.; Lee, G. S.; Davis, M. E.; Elomari, S.; Medrud, R. C.; Zones, S. I. Guest/Host Relationships in the Synthesis of the Novel Cage-Based Zeolites SSZ-35, SSZ-36, and SSZ-39. *J. Am. Chem. Soc.* **2000**, *122*, 263–273.

(11) Lewis, D. W.; Freeman, C. M.; Catlow, C. R. A. Predicting the Templating Ability of Organic Additives for the Synthesis of Microporous Materials. *J. Phys. Chem.* **1995**, *99*, 11194–11202.

(12) Burton, A. W.; Lee, G. S.; Zones, S. I. Phase selectivity in the syntheses of cage-based zeolite structures: An investigation of thermodynamic interactions between zeolite hosts and structure directing agents by molecular modeling. *Microporous Mesoporous Mater.* **2006**, *90*, 129–144.

(13) Pophale, R.; Daeyaert, F.; Deem, M. W. Computational prediction of chemically synthesizable organic structure directing agents for zeolites. *J. Mater. Chem. A* **2013**, *1*, 6750–6760.

(14) Schmidt, J. E.; Deem, M. W.; Lew, C.; Davis, T. M. Computationally-Guided Synthesis of the 8-Ring Zeolite AEI. *Top. Catal.* **2015**, *58*, 410–415.

(15) Davis, T. M.; Liu, A. T.; Lew, C. M.; Xie, D.; Benin, A. I.; Elomari, S.; Zones, S. I.; Deem, M. W. Computationally Guided Synthesis of SSZ-52: A Zeolite for Engine Exhaust Clean-up. *Chem. Mater.* **2016**, *28*, 708–711.

(16) Schmidt, J. E.; Deem, M. W.; Davis, M. E. Synthesis of a Specified, Silica Molecular Sieve by Using Computationally Predicted Organic Structure-Directing Agents. *Angew. Chem. Int. Ed.* **2014**, *53*, 8372–8374.

(17) Muraoka, K.; Chaikittisilp, W.; Okubo, T. Multi-objective de novo molecular design of organic structure-directing agents for zeolites using nature-inspired ant colony optimization. *Chem. Sci.* **2020**, *11*, 8214–8223.

(18) Schwalbe-Koda, D.; Gómez-Bombarelli, R. Benchmarking binding energy calculations for organic structure-directing agents in pure-silica zeolites. *J. Chem. Phys.* **2021**, *154*, 174109.

(19) Waitt, C.; Gao, X.; Gounder, R.; Debellis, A.; Prasad, S.; Moini, A.; Schneider, W. F. Analysis and Augmentation of Guest–Host Interaction Energy Models as CHA and AEI Zeolite Crystallization Phase Predictors. *J. Phys. Chem. C* **2023**, *127*, 22740–22751.

(20) Dusselier, M.; Davis, M. E. Small-Pore Zeolites: Synthesis and Catalysis. *Chem. Rev.* **2018**, *118*, 5265–5329.

(21) Knott, B. C.; Nimlos, C. T.; Robichaud, D. J.; Nimlos, M. R.; Kim, S.; Gounder, R. Consideration of the Aluminum Distribution in Zeolites in Theoretical and Experimental Catalysis Research. *ACS Catalysis* **2018**, *8*, 770–784.

(22) Le, T. T.; Chawla, A.; Rimer, J. D. Impact of acid site speciation and spatial gradients on zeolite catalysis. *Journal of Catalysis* **2020**, *391*, 56–68.

(23) Kester, P. M.; Crum, J. T.; Li, S.; Schneider, W. F.; Gounder, R. Effects of Brønsted acid site proximity in chabazite zeolites on OH infrared spectra and protolytic propane cracking kinetics. *Journal of Catalysis* **2021**, *395*, 210–226.

(24) Shan, Y.; Du, J.; Zhang, Y.; Shan, W.; Shi, X.; Yu, Y.; Zhang, R.; Meng, X.; Xiao, F.-S.; He, H. Selective catalytic reduction of NOx with NH3: opportunities and challenges of Cu-based small-pore zeolites. *National Science Review* **2021**, *8*, nwab010.

(25) Li, S.-C.; Lin, Y.-C.; Li, Y.-P. Understanding the Catalytic Activity of Microporous

and Mesoporous Zeolites in Cracking by Experiments and Simulations. *Catalysts* **2021**, *11*, 1114.

(26) Di Iorio, J. R.; Nimlos, C. T.; Gounder, R. Introducing Catalytic Diversity into Single-Site Chabazite Zeolites of Fixed Composition via Synthetic Control of Active Site Proximity. *ACS Catal.* **2017**, *7*, 6663–6674.

(27) Paolucci, C.; Verma, A. A.; Bates, S. A.; Kispersky, V. F.; Miller, J. T.; Gounder, R.; Delgass, W. N.; Ribeiro, F. H.; Schneider, W. F. Isolation of the Copper Redox Steps in the Standard Selective Catalytic Reduction on Cu-SSZ-13. *Angew. Chem. Int. Ed.* **2014**, *53*, 11828–11833.

(28) Ipek, B.; Wulfers, M. J.; Kim, H.; Göltl, F.; Hermans, I.; Smith, J. P.; Booksh, K. S.; Brown, C. M.; Lobo, R. F. Formation of [Cu2O2]2+ and [Cu2O]2+ toward C–H Bond Activation in Cu-SSZ-13 and Cu-SSZ-39. *ACS Catal.* **2017**, *7*, 4291–4303.

(29) Deimund, M. A.; Harrison, L.; Lunn, J. D.; Liu, Y.; Malek, A.; Shayib, R.; Davis, M. E. Effect of Heteroatom Concentration in SSZ-13 on the Methanol-to-Olefins Reaction. *ACS Catal.* **2016**, *6*, 542–550.

(30) Shantz, D.; Lobo, R.; Fild, C.; Koller, H. In *12th International Congress on Catalysis*; Corma, A., Melo, F. V., Mendioroz, S., Fierro, J. L. G., Eds.; Studies in Surface Science and Catalysis; Elsevier, 2000; Vol. 130; pp 845–850.

(31) Sabater, M. J.; Sastre, G. A Computational Study on the Templating Ability of the Trispyrrolidinium Cation in the Synthesis of ZSM-18 Zeolite. *Chem. Mater.* **2001**, *13*, 4520–4526.

(32) Sastre, G.; Fornes, V.; Corma, A. On the Preferential Location of Al and Proton Siting in Zeolites: A Computational and Infrared Study. *J. Phys. Chem. B* **2002**, *106*, 701–708.

(33) Pinar, A. B.; Gómez-Hortigüela, L.; McCusker, L. B.; Pérez-Pariente, J. Controlling the Aluminum Distribution in the Zeolite Ferrierite via the Organic Structure Directing Agent. *Chem. Mater.* **2013**, *25*, 3654–3661.

(34) Muraoka, K.; Chaikittisilp, W.; Yanaba, Y.; Yoshikawa, T.; Okubo, T. Directing Aluminum Atoms into Energetically Favorable Tetrahedral Sites in a Zeolite Framework by Using Organic Structure-Directing Agents. *Angew. Chem. Int. Ed.* **2018**, *57*, 3742–3746.

(35) Toyoda, H.; Osuga, R.; Wang, Y.; Park, S.; Yazawa, K.; Gies, H.; Gilbert, C. J.; Yilmaz, B.; Kelkar, C. P.; Yokoi, T. Clarification of acid site location in MSE-type zeolites by spectroscopic approaches combined with catalytic activity: comparison between UZM-35 and MCM-68. **2022**, *24*, 4358–4365.

(36) de Vos Burchart, E.; Jansen, J. C.; van de Graaf, B.; van Bekkum, H. Molecular mechanics studies on MFI-typezeolites: Part 4. Energetics of crystal growth directing agents. *Zeolites* **1993**, *13*, 216–221.

(37) Yokoi, T.; Mochizuki, H.; Namba, S.; Kondo, J. N.; Tatsumi, T. Control of the Al Distribution in the Framework of ZSM-5 Zeolite and Its Evaluation by Solid-State NMR Technique and Catalytic Properties. *J. Phys. Chem. C* **2015**, *119*, 15303–15315.

(38) Nimlos, C. T.; Hoffman, A. J.; Hur, Y. G.; Lee, B. J.; Di Iorio, J. R.; Hibbitts, D. D.; Gounder, R. Experimental and Theoretical Assessments of Aluminum Proximity in MFI Zeolites and Its Alteration by Organic and Inorganic Structure-Directing Agents. *Chem. Mater.* **2020**, *32*, 9277–9298.

(39) Ezenwa, S.; Montalvo-Castro, H.; Hoffman, A. J.; Locht, H.; Attebery, J.; Jan, D.-Y.; Schmithorst, M.; Chmelka, B.; Hibbitts, D.; Gounder, R. Synthetic Placement of Active Sites in MFI Zeolites for Selective Toluene Methylation to para-Xylene. *J. Am. Chem. Soc.* **2024**, *146*, 10666–10678.

(40) Di Iorio, J. R.; Gounder, R. Controlling the Isolation and Pairing of Aluminum in Chabazite Zeolites Using Mixtures of Organic and Inorganic Structure-Directing Agents. *Chem. Mater.* **2016**, *28*, 2236–2247.

(41) Di Iorio, J. R.; Li, S.; Jones, C. B.; Nimlos, C. T.; Wang, Y.; Kunkes, E.; Vattipalli, V.; Prasad, S.; Moini, A.; Schneider, W. F.; Gounder, R. Cooperative and Competitive Occlusion of Organic and Inorganic Structure-Directing Agents within Chabazite Zeolites Influences Their Aluminum Arrangement. *J. Am. Chem. Soc.* **2020**, *142*, 4807–4819.

(42) Zhang, J.; Shan, Y.; Zhang, L.; Du, J.; He, H.; Han, S.; Lei, C.; Wang, S.; Fan, W.; Feng, Z.; Liu, X.; Meng, X.; Xiao, F.-S. Importance of controllable Al sites in CHA framework by crystallization pathways for NH3-SCR reaction. *Appl. Catal., B* **2020**, *277*, 119193.

(43) Gallego, E. M.; Li, C.; Paris, C.; Martín, N.; Martínez-Triguero, J.; Boronat, M.; Moliner, M.; Corma, A. Making Nanosized CHA Zeolites with Controlled Al Distribution for Optimizing Methanol-to-Olefin Performance. *Chem. Eur. J.* **2018**, *24*, 14631–14635.

(44) Lee, S.; Nimlos, C. T.; Kipp, E. R.; Wang, Y.; Gao, X.; Schneider, W. F.; Lusardi, M.; Vattipalli, V.; Prasad, S.; Moini, A.; Gounder, R. Evolution of Framework Al Arrangements in CHA Zeolites during Crystallization in the Presence of Organic and Inorganic Structure-Directing Agents. *Cryst. Growth Des.* **2022**, *22*, 6275–6295.

(45) Lv, W.; Wang, S.; Wang, P.; Liu, Y.; Huang, Z.; Li, J.; Dong, M.; Wang, J.; Fan, W. Regulation of Al distributions and Cu2+ locations in SSZ-13 zeolites for NH3-SCR of NO by different alkali metal cations. *J. Catal.* **2021**, *393*, 190–201.

(46) Fletcher, R. E.; Ling, S.; Slater, B. Violations of Löwenstein's rule in zeolites. *Chem. Sci.* **2017**, *8*, 7483–7491.

(47) Li, S.; Li, H.; Gounder, R.; Debellis, A.; Müller, I. B.; Prasad, S.; Moini, A.; Schneider, W. F. First-Principles Comparison of Proton and Divalent Copper Cation Ex-

change Energy Landscapes in SSZ-13 Zeolite. *J. Phys. Chem. C* **2018**, *122*, 23564–23573.

(48) Li, S.; Gounder, R.; Debellis, A.; Müller, I. B.; Prasad, S.; Moini, A.; Schneider, W. F. Influence of the N,N,N-Trimethyl-1-adamantyl Ammonium Structure-Directing Agent on Al Substitution in SSZ-13 Zeolite. *J. Phys. Chem. C* **2019**, *123*, 17454–17458.

(49) Wang, X.; Wang, Y.; Moini, A.; Gounder, R.; Maginn, E. J.; Schneider, W. F. Influence of an N,N,N-Trimethyl-1-adamantyl Ammonium (TMAda+) Structure Directing Agent on Al Distributions and Pair Features in Chabazite Zeolite. *Chem. Mater.* **2022**, *34*, 10811–10822.

(50) Tang, X.; Liu, Z.; Huang, L.; Chen, W.; Li, C.; Wang, G.; Li, G.; Yi, X.; Zheng, A. Violation or Abidance of Löwenstein's Rule in Zeolites Under Synthesis Conditions? *ACS Catal.* **2019**, *9*, 10618–10625.

(51) Loewenstein, W. The distribution of aluminum in the tetrahedra of silicates and aluminates. *American Mineralogist* **1954**, *39*, 92–96.

(52) Oishi, K.; Muraoka, K.; Nakayama, A. Analysis of Al site-directing ability of organic structure-directing agents in FER and CHA zeolites: a computational exploration of energetic preferences. *Chem. Commun.* **2023**, *59*, 8953–8956.

(53) Kresse, G.; Furthmüller, J. Efficient iterative schemes for ab initio total-energy calculations using a plane-wave basis set. *Phys. Rev. B* **1996**, *54*, 11169.

(54) Blöchl, P. E. Projector Augmented-Wave Method. *Phys. Rev. B* **1994**, *50*, 17953.

(55) Perdew, J. P.; Burke, K.; Ernzerhof, M. Generalized Gradient Approximation Made Simple. *Phys. Rev. Lett.* **1996**, *77*, 3865.

(56) Grimme, S.; Ehrlich, S.; Goerigk, L. Effect of the damping function in dispersion corrected density functional theory. *J. Comput. Chem.* **2011**, *32*, 1456–1465.

(57) Frisch, M. J. et al. Gaussian˜16 Revision C.01. 2016; Gaussian Inc. Wallingford CT.

(58) Grau-Crespo, R.; Hamad, S.; Catlow, C. R. A.; Leeuw, N. H. d. Symmetry-adapted configurational modelling of fractional site occupancy in solids. *J. Phys.: Condens. Matter* **2017**, *19*, 256201.

(59) Hanwell, M. D.; Curtis, D. E.; Lonie, D. C.; Vandermeersch, T.; Zurek, E.; Hutchison, G. R. Avogadro: an advanced semantic chemical editor, visualization, and analysis platform. *J. Cheminf.* **2012**, *4*, 17.

(60) Larsen, A. H. et al. The atomic simulation environment—a Python library for working with atoms. *J. Phys.: Condens. Matter* **2017**, *29*, 273002.

(61) Crum, J. T.; Crum, J. R.; Taylor, C.; Schneider, W. F. Characterization and analysis of ring topology of zeolite frameworks. *Microporous Mesoporous Mater. 351*, 112466.

(62) Crum, J. Zeolite Simulation Environment. `https://github.com/jtcrum/zse`, (Accessed: December 2023).

(63) Gao, X.; Schneider, W. F. Structure Databases: Predicted Influence of Organic Structure Directing Agents on Al Distributions in CHA Zeolites. `https://doi.org/10.5281/zenodo.13236661`, (Accessed: August 2024).

(64) Schwalbe-Koda, D.; Kwon, S.; Paris, C.; Bello-Jurado, E.; Jensen, Z.; Olivetti, E.; Willhammar, T.; Corma, A.; Román-Leshkov, Y.; Moliner, M.; Gómez-Bombarelli, R. A priori control of zeolite phase competition and intergrowth with high-throughput simulations. *Science* **2021**, *374*, 308–315.

(65) Wilcox, L. N.; Rebolledo-Oyarce, J.; Mikes, A. D.; Wang, Y.; Schneider, W. F.; Gounder, R. Structure and Reactivity of Binuclear Cu Active Sites in Cu-CHA Zeolites for Stoichiometric Partial Methane Oxidation to Methanol. *ACS Catalysis* **2024**, *14*, 3647–3663.

(66) Krishna, S. H.; Goswami, A.; Wang, Y.; Jones, C. B.; Dean, D. P.; Miller, J. T.; Schneider, W. F.; Gounder, R. Influence of framework Al density in chabazite zeolites on copper ion mobility and reactivity during NOx selective catalytic reduction with NH3. *Nature Catalysis* **2023**, *6*, 276–285.

(67) Deng, L. et al. Atom-Economic Synthesis of Zeolites. *J. Am. Chem. Soc.* [Advance online publication], Available at: https://doi.org/10.1021/jacs.4c11264.

TOC Graphic

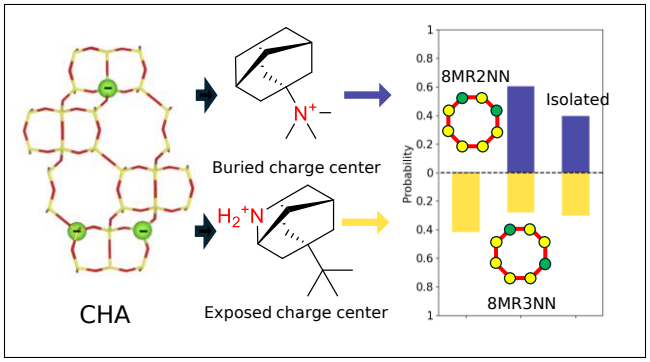
CHA
Buried charge center
Exposed charge center
8MR2NN
Isolated
8MR3NN
Probability